

Finescale Structure of the LaGrange, Wyoming, Tornado during VORTEX2: GBVTD and Photogrammetric Analyses

ROGER M. WAKIMOTO, PHILLIP STAUFFER, AND WEN-CHAU LEE

National Center for Atmospheric Research, Boulder, Colorado*

NOLAN T. ATKINS

Department of Atmospheric Sciences, Lyndon State College, Lyndonville, Vermont

JOSHUA WURMAN

Center for Severe Weather Research, Boulder, Colorado

(Manuscript received 29 January 2012, in final form 1 May 2012)

ABSTRACT

A ground-based velocity track display (GBVTD) analysis of the LaGrange, Wyoming, tornado on 5 June 2009 during the Second Verification of the Origins of Rotation in Tornadoes Experiment (VORTEX2) is photogrammetrically combined with a series of pictures of the funnel cloud. This analysis reveals the relationship between the vertical velocity, radial and tangential velocities, perturbation pressure, vertical vorticity, and angular momentum with the visual features of the tornado. An intense axial downdraft was evident and was supported by a downward-directed perturbation pressure gradient. The radial inflow at low levels was weak and difficult to retrieve owing to a combination of centrifuging of hydrometeors/debris in the intense circulation and the inability of the radar beam to fully resolve the flow. The tornado was weakening during the analysis period, which was supported by angular momentum being advected out of the tornado.

The availability of a dual-Doppler wind synthesis for this tornadic event provided a unique opportunity to assess the assumptions in the GBVTD methodology. The analysis suggests that the simplified GBVTD equations that have been applied in past studies of tornadoes are not appropriate in the present case. The most accurate retrieval of the radial velocities requires that a higher-order term that is typically neglected be retained. A quantitative assessment of the impact of centrifuging of hydrometeors on the synthesized wind field was attempted. The results suggest that the radial and vertical velocity profile near and within the tornado core can be significantly altered for tornadoes (EF2) that are accompanied by a small radius of maximum wind and relatively weaker low-level inflow.

1. Introduction

Radar has been one of the most important observational platforms used in studying tornadoes and tornadic storms. The hook echo, mesocyclone, and tornadic-vortex signature (TVS) are common radar signatures noted in many past studies and have increased our understanding

of these strong circulations (e.g., Stout and Huff 1953; Brown et al. 1978; Zrnic and Istok 1980; Forbes 1981; Burgess et al. 2002). The introduction of mobile Doppler radars (X and W band) has allowed researchers to collect high-resolution reflectivity and velocity data of these features with unprecedented detail (e.g., Bluestein et al. 1993, 1997, 2004, 2007a,b; Wurman et al. 1996; Wurman and Gill 2000; Alexander and Wurman 2005; Wurman et al. 2007a). In recent years, researchers have been adept at strategically deploying two or more mobile radars near the hook echo in order to collect dual-Doppler data of tornadoes and the surrounding wind field (e.g., Wurman et al. 2007a,b, 2010a; Marquis et al. 2008). The radars are typically deployed 7–10 km from the tornadoes resulting in data interpolation onto a Cartesian grid of $O[100 \text{ m}]$.

* The National Center for Atmospheric Research is sponsored by the National Science Foundation.

Corresponding author address: Roger M. Wakimoto, NCAR, P.O. Box 3000, Boulder, CO 80307.
E-mail: wakimoto@ucar.edu

The data spacing is appropriate for divergence and vorticity analyses of the kinematic fields within the low-level mesocyclone (e.g., Wurman et al. 2007a, 2010a; Marquis et al. 2008) but is still insufficient to fully resolve the actual tornado circulation unless it is 1 km or larger (e.g., Carbone et al. 1985). Indeed, Wurman et al. (2007a) have suggested that successes in deploying multiple radars with short baselines required for resolving tornadic vortices in a dual-Doppler wind synthesis may be so infrequent as to be unfeasible.

The limit imposed by the minimum resolvable scale in a dual-Doppler wind synthesis has led to an exploration of alternative methods that could effectively utilize the finescale, single-Doppler velocity data to reconstruct the three-dimensional wind field associated with the tornado. One of the techniques that appears to hold the most promise is the ground-based velocity track display technique (GBVTD; Lee et al. 1999), originally developed to retrieve the wind fields within tropical cyclones using single-Doppler data. The GBVTD technique takes advantage of the near-circular nature of the vortex and deduces the wind field of the circulation using a decomposition similar to the velocity azimuth display (VAD) technique (Browning and Wexler 1968). Simplified versions of the GBVTD methodology have been proposed by Dowell et al. (2005) and Rasmussen and Straka (2007) and applied by Kosiba et al. (2008) in the study of tornadoes. The GBVTD technique has been used to resolve the two-dimensional (Bluestein et al. 2003, 2007a; Tanamachi et al. 2007) and three-dimensional (Lee and Wurman 2005; Kosiba and Wurman 2010) wind field of a tornado circulation. The kinematic structure of the circulation presented in the latter two studies have produced datasets that are approaching the detailed wind fields revealed in recent large eddy simulations of tornadoes (e.g., Lewellen et al. 2000; Lewellen and Lewellen 2007a,b). Missing from these past analyses is a comparison between the wind fields reconstructed from dual-Doppler and GBVTD techniques for the same tornadic event. This comparison would help assess the validity of the GBVTD assumptions used in deriving the wind field.

It is common for a tornado's life cycle to be well documented with both video and still photography (e.g., Bluestein 1999). A careful analysis of photographs taken of the tornado at the same time as radar data collection, however, has been relatively rare (Bluestein et al. 1993, 1997, 2004, 2007a,b; Tanamachi et al. 2007, Wakimoto et al. 2003). Photogrammetric analysis has been used to obtain information about the visual characteristics of the tornado (e.g., width of the condensation funnel) that cannot be determined with microwave radars that are insensitive to small cloud drops. Wurman et al. (2007b), Kosiba et al. (2008), Marquis et al. (2008), and Kosiba

and Wurman (2010) present high-resolution Doppler radar analyses but there was no documentation of the visual features of the tornadoes. Photographs of the tornado are shown in Wurman and Gill (2000) and Wurman et al. (2007a, 2010a) but no quantitative information of the visual features were discussed. Rasmussen and Straka (2007) superimposed interpolated radar reflectivity onto tornado photos at three separate times. Interpolated radar reflectivity and single-Doppler velocity data were placed on top of a picture of an intense tornado by Dowell et al. (2005) but only for a single time. Wakimoto et al. (2003) combined analysis of radar reflectivity, dual-Doppler wind syntheses, vertical velocity and vorticity, and perturbation pressure onto a tornado photograph but at coarse resolution. Wakimoto and Martner (1992) provided a photogrammetric and Doppler radar analysis of the entire life cycle of a Colorado tornado; however, it was associated with a nonsupercell storm (i.e., the tornado was not associated with a mesocyclone).

A fundamental assumption of kinematic analyses using Doppler velocity data is that the scatterers are moving with the horizontal wind field. However, hydrometeors/debris within an intense tornadic circulation can undergo centrifuging (e.g., Snow 1984; Wurman and Gill 2000; Dowell et al. 2005). Centrifuging produces a positive bias in the radial velocity calculations leading to, among other effects, an underestimate of the radial inflow into the tornado at low levels. Even though this contamination of the Doppler velocity field is well known, to date there has been no attempt to quantitatively assess the impact of this centrifuging on retrieved wind fields.

An opportunity to address the issues described in the preceding paragraphs was possible during a major field campaign deployed in the Midwest. A tornado developed west of LaGrange, Wyoming, on 5 June 2009 during the Second Verification of the Origins of Rotation in Tornadoes Experiment (VORTEX2). VORTEX2 was a multi-agency field project that operated during the springs of 2009/10 and was focused on collecting high-resolution data on tornadoes and tornadic storms (Wurman et al. 2010b). A novel aspect of this experiment was the large number of mobile observational platforms and no single home base for operations during the entire field campaign. Several radars collected data on the LaGrange tornado while the visual evolution of the funnel was captured by a series of photographs and high-definition video. The primary dataset used in the study was collected by the Doppler-on-Wheels (DOWs; Wurman et al. 1997; Wurman 2001). In an earlier study, single-Doppler radar data were combined with these photographs in an attempt to relate the hook echo and rotational couplet to the visual characteristics of the tornado (Wakimoto et al. 2011). The three-dimensional kinematic field based on

a dual-Doppler wind synthesis was merged with the photographs in a subsequent analysis (Atkins et al. 2012). The purpose of this merger was to document the relationship between the profiles of vertical vorticity, circulation, and angular momentum with the tornado and the wall cloud.

The present study is the first time that a tornadic circulation that is resolved by the GBVTD analysis has been superimposed onto a series of photographs of the funnel. In addition, dual-Doppler wind syntheses were available for this event. The latter kinematic analyses are detailed but are still unable to resolve the tornado wind field. The existence of both wind fields, however, provides a unique opportunity to assess the assumptions in the GBVTD methodology and also provide guidance for future mobile radar deployments around supercell storms. The DOW radars and cloud photogrammetry are presented in section 2. Section 3 discusses the GBVTD technique. A description of the deployment of the radars and an overview of the hook echo is shown in section 4. Section 5 presents the GBVTD analysis of the LaGrange tornado and section 6 provides an assessment of the centrifuging of hydrometeors in introducing a positive bias in the radial velocity estimate. A summary and discussion are presented in section 7.

2. DOW radars and cloud photogrammetry

The radar data collected by the DOWs (DOW6 and DOW7) are used in this study. The 3-cm wavelength radars are mounted on trucks and have been used extensively to collect data near tornadoes. The DOWs peak transmitted power is 250 kW. The radars scanned at 50° s^{-1} , employed 250-ns pulses at 4000-Hz pulse repetition frequency, and sampled returned signals to retrieve 60-m gate spacing. The radar half-power beamwidth is 0.93° . The radar reflectivity and Doppler velocity values for DOW7 were calibrated to within ± 2 dBZ and 1 m s^{-1} , respectively. The dual-Doppler coordinated volume scans occurred every 2 min and the elevation scans (0.5° , 1° , 2° , 3° , 4° , 5° , 6° , 8° , 10° , 12° , 14° , and 16°) collected detailed data on the structure of the tornado. The DOW6 and DOW7 reflectivity and Doppler velocity data were navigated using ground clutter targets. The data were also edited and dealiased using the SOLO software (Oye et al. 1995). For more information about the DOWs, the interested reader is referred to Wurman et al. (1997) and Wurman (2001).

Quantitative information can be derived from pictures of a tornado using photogrammetric analysis (e.g., Malkus 1952; Rasmussen et al. 2003; Zehnder et al. 2007). The first step in photogrammetry is determining the location of the camera and the azimuth angles of several

targets identified in the horizon shown in the picture. The effective focal length and the tilt angle of the camera can subsequently be determined using spherical trigonometry. These parameters are then used to construct an elevation- and azimuth-angle grid that can be superimposed on top of the photograph. The calculated azimuth angles were compared with known targets identified in the picture to assess the accuracy of the grid. This analysis suggests that errors range between 0.1° and 0.2° . An overview of photogrammetry can be found in Abrams (1952) and Holle (1986). Additional details of the technique used to analyze the photos shown in this paper are presented in Wakimoto et al. (2011).

3. GBVTD technique

The full formulation of the GBVTD methodology can be found in Lee et al. (1999). The GBVTD technique assumes that the circulation is characterized by a quasi-axisymmetric structure. The data are adjusted to a common time using an advection correction based on the mesocyclone motion (12 m s^{-1} from 275°). The tornado motion is subtracted from the radial wind fields. The radial velocity data are interpolated onto a Cartesian grid using a bilinear interpolation algorithm. A series of analysis rings at different radii are created and centered on the circulation. The center of the circulation is objectively located using a methodology outlined in Lee and Marks (2000) for each level. A least squares fit up to angular wavenumber 3 of the radial velocity data at each radius is then applied. Higher-order wavenumber artifacts that might be created by the bilinear interpolation would be filtered during this step.

Using the Fourier decomposition, Lee et al. (1999) illustrate how the axisymmetric tangential and radial winds result in a simple sine curve with a phase shift. Actual circulations are asymmetric and are composed of a mean flow and waves of all forms. The asymmetry results in a complex waveform that can be decomposed into Fourier components. The Fourier coefficients of the vortex circulation, however, cannot be uniquely derived since the equation is underdetermined. $V_R C_n$ and $V_T C_n$ ($V_R S_n$ and $V_T S_n$) are defined as the amplitude of the cosine (sine) components of the tangential velocity (V_T) and radial velocity (V_R), respectively, for angular wavenumber n (hereafter, angular wavenumber is referred to as wavenumber). Lee et al. (1999) have shown that $V_T C_0$ and $V_R C_0$ can be represented by the following equations:

$$V_T C_0 = -B_1 - B_3 - V_M \sin(\theta_T - \theta_M) \sin \alpha_{\max} + V_R S_2, \quad (1)$$

$$V_R C_0 = A_1 + A_3 - V_R C_2, \quad (2)$$

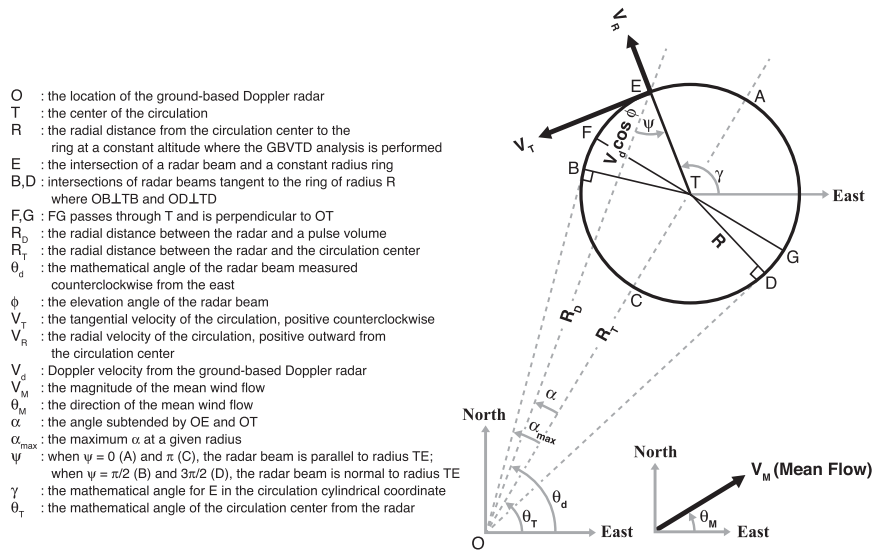


FIG. 1. The geometry used in a GBVTD analysis. Based on a figure from Lee et al. (1999).

where V_M represents the mean flow; and A_1 , A_3 , B_1 , and B_3 are the Fourier coefficients for wavenumbers 1 and 3 of the Doppler velocities analyzed on each radius. The basic geometry for the GBVTD analysis is shown in Fig. 1. Here θ_M and θ_T are the angles measured from due east of the mean flow and the center of the circulation relative to the radar location, respectively; α_{max} is the angular distance (relative to the radar location) measured from the center of the circulation to the tangent of the analysis ring under consideration; and $V_M \sin(\theta_T - \theta_M)$ is the component of V_M that is perpendicular to the line drawn from the radar location through the center of the circulation (i.e., perpendicular to the radar beam that passes through the center of the circulation).

Lee et al. (1994) proposed the closure assumption that the asymmetric radial velocity (V_R) was much smaller than the corresponding tangential velocity (V_T). As a result, the $V_R S_2$ and $V_R C_2$ terms are ignored in (1) and (2), respectively. In the single-Doppler methodology, $V_M \sin(\theta_T - \theta_M)$ cannot be measured and is assumed to be small compared to the other terms. The end products of this procedure are the axisymmetric mean (hereafter referred to as the mean) tangential and radial winds and asymmetric tangential winds for each level. The mean divergence, vertical velocity (based on an upward integration of divergence), vertical vorticity, and angular momentum can be calculated. The perturbation pressure gradient associated with the primary circulation can also be determined.

Dual-Doppler wind syntheses based on the data collected by the DOW6 and DOW7 radars were available for this case and allow for a direct estimate of the three ignored terms in (1) and (2). The reflectivity and velocity

information were interpolated onto a Cartesian grid and an advection correction based on the mesocyclone motion was used to adjust the data to a common time. The objective analysis employed a two-pass Barnes filter. The multipass analysis has been shown to result in less damping at well-resolved wavelengths than single-pass objective analyses while still suppressing small-scale noise (Majcen et al. 2008). The maximum range from both radars to the tornado was 20 km. Data were oversampled in the azimuthal direction (0.7°) resulting in a maximum horizontal data spacing (δ) of 244 m. The resultant smoothing parameter ($\kappa_o = 0.48 \text{ km}^2$) was 0.106 km^2 (Pauley and Wu 1990). The horizontal and vertical grid spacing was chosen to be 100 m ($\delta/2.5$; Koch et al. 1983). Vertical velocities were derived from an upward integration of the continuity equation.

Range–height profiles of the axisymmetric V_R for 2216:08–2216:45 UTC are shown in Fig. 2. The profile of V_R based on the azimuthally averaged, dual-Doppler wind synthesis is presented in Fig. 2a. The GBVTD analysis of V_R ignoring the $V_R C_2$ term is shown in Fig. 2b. The GBVTD analysis is able to resolve smaller wavelengths so the field shown in Fig. 2b has been filtered to match the resolvable scales based on the dual-Doppler wind synthesis.¹ There is a major difference between

¹ The filtering applied to the dual-Doppler wind synthesis resulted in 50% and 80% of the wave energy at scales greater than 0.63 and 0.95 km, respectively, being resolved. The dual-Doppler wind synthesis at these scales was not able to fully resolve the tornadic circulation. In addition, this filtering would largely remove the effects of centrifuging (discussed in section 6) in the dual-Doppler wind syntheses.

2216:08 - 2216:45

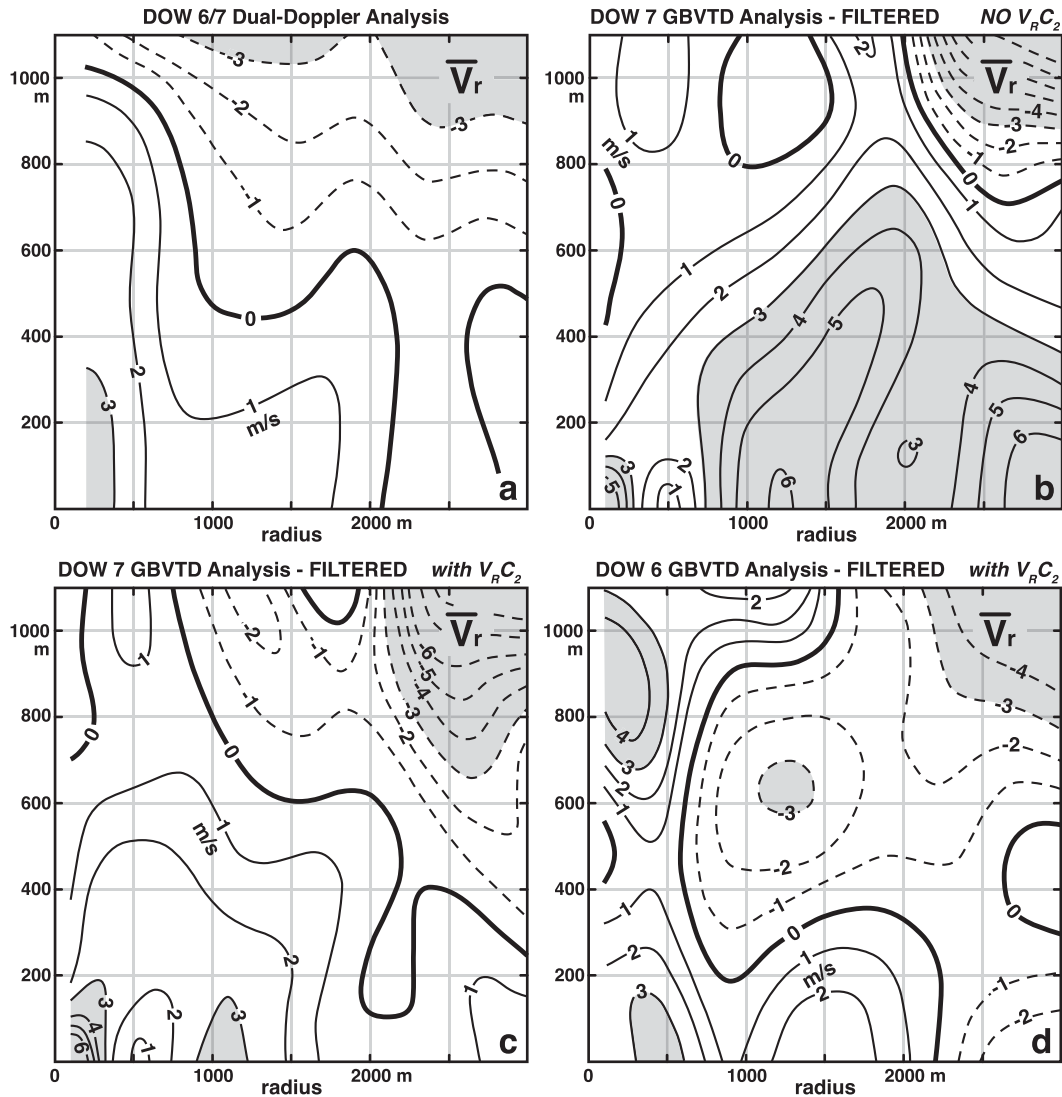


FIG. 2. Range–height cross section of the axisymmetric radial velocities for 2216:08–2216:45 UTC for the LaGrange tornado. (a) Based on the azimuthally averaged dual-Doppler wind synthesis using data collected by DOW6 and DOW7. (b) Based on a GBVTD analysis using data collected by DOW7 and filtered to resolve wavelengths similar to the dual-Doppler wind syntheses. The $V_R C_2$ term has been ignored in this calculation. (c) As in (b), but including the $V_R C_2$ term estimated from the dual-Doppler analysis. (d) As in (c), but for DOW6. Values $>3 \text{ m s}^{-1}$ or $<-3 \text{ m s}^{-1}$ are shaded gray.

GBVTD estimate of V_R based on the single-Doppler data collected by DOW7 and the dual-Doppler wind synthesis. The GBVTD analysis including the effect of the $V_R C_2$ term derived from the dual-Doppler wind synthesis at 2216:08–2216:45 UTC (Fig. 2c) largely replicates the main features that are apparent in Fig. 2a. The stronger values in the GBVTD analysis are a result of higher-resolution data collected by the DOW7 radar. The filtered GBVTD analysis based on data collected by DOW6 (and including the $V_R C_2$ term) is shown in Fig. 2d.

Although there is broad similarities between the fields shown in Figs. 2a,d, the agreement is not as good as the DOW7 analysis. These differences are likely the result of the greater distance between the DOW6 site and the tornado.

The profiles presented in Fig. 2 are an example where some of the assumptions discussed by Lee et al. (1999) are not valid. That is, the axisymmetric radial velocities are not significantly larger than the asymmetric radial velocities (represented by the higher-order

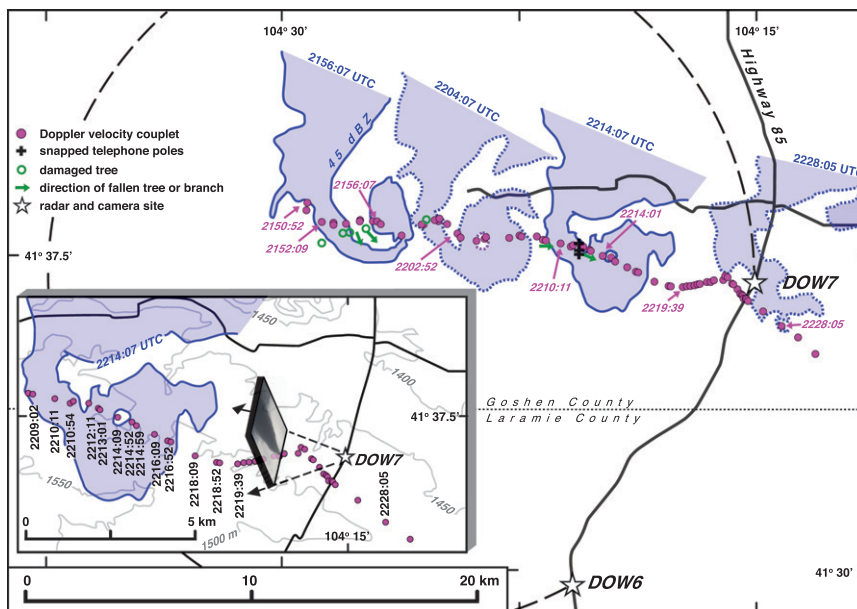


FIG. 3. Hook echo (1° elevation angle) associated with the LaGrange supercell storm at 2156:07, 2204:07, 2214:07, and 2228:05 UTC recorded from the DOWs. Magenta dots represent the location of the tornadic rotational couplet based on low-level scans. Damage to telephone poles and trees are plotted (explanation of the symbols are shown in the legend). An enlargement near DOW7 is shown in the inset. The times of the rotational couplet observations are labeled on the figure. A schematic illustrating the series of photographs taken from the DOW7 site is also shown. The gray lines are the height of the topography. The locations of DOW6 and DOW7 are shown by the stars. The primary dual-Doppler lobe is plotted. The radar reflectivity values greater than 45 dBZ are shaded blue.

wavenumbers). It can be seen in (1) and (2) that the unresolved wavenumber-2 radial wind component directly biases the mean tangential and radial winds of the vortex. In strong tornadoes (e.g., Lee and Wurman 2005), the assumption used in Lee et al. (1999) is appropriate. In the present case, however, the wavenumber-2 radial wind component is of the same order of magnitude as the mean radial wind and the $V_R C_2$ term in (2) should not be ignored. Accordingly, the radial velocity profiles plotted in section 5 were derived from the full equation shown in (2) using the wavenumber-2 component estimated from the dual-Doppler wind synthesis as a proxy. The validity of adding a smoothed wavenumber-2 parameter to the GBVTD analysis was partially addressed by recomputing the $V_R C_2$ term using higher-resolution dual-Doppler wind syntheses (i.e., filter the wind synthesis such that smaller scales were resolved, including an extreme case where no filter was applied). The retrieved $V_R C_2$ fields based on these alternative wind fields produced similar fields (not shown) that would not have altered any of the conclusions presented in this paper.

The axisymmetric tangential velocities were calculated by azimuthally averaging the dual-Doppler wind

syntheses (not shown). These velocities were also estimated using the GBVTD technique using the single-Doppler velocities recorded by DOW7 and neglecting the mean flow perpendicular to the radar beam [$V_M \sin(\theta_T - \theta_M)$] and the $V_R S_2$ terms in (1). The mean tangential velocities were also calculated by including the latter two terms by using the dual-Doppler wind field (not shown). The GBVTD analyses were filtered to match the resolvable scales based on the dual-Doppler wind synthesis similar to the results shown in Fig. 2. The comparison of the range–height profiles (not shown) revealed a close agreement between the GBVTD and dual-Doppler estimates of the mean tangential velocities. This analysis validates the original closure assumption proposed by Lee et al. (1994). As a result, the axisymmetric tangential velocity profiles shown in section 5 used the simplified version of (1) that neglect the last two terms on the right-hand side of the equation.

GBVTD analyses were performed during the 2216 and 2218 UTC volume scans by the DOW7 radar. The tornado was approximately 5.5 and 3.6 km from the radar during these times, respectively. These distances were deemed close enough that the tornadic circulation could be reconstructed by the GBVTD technique. Earlier times

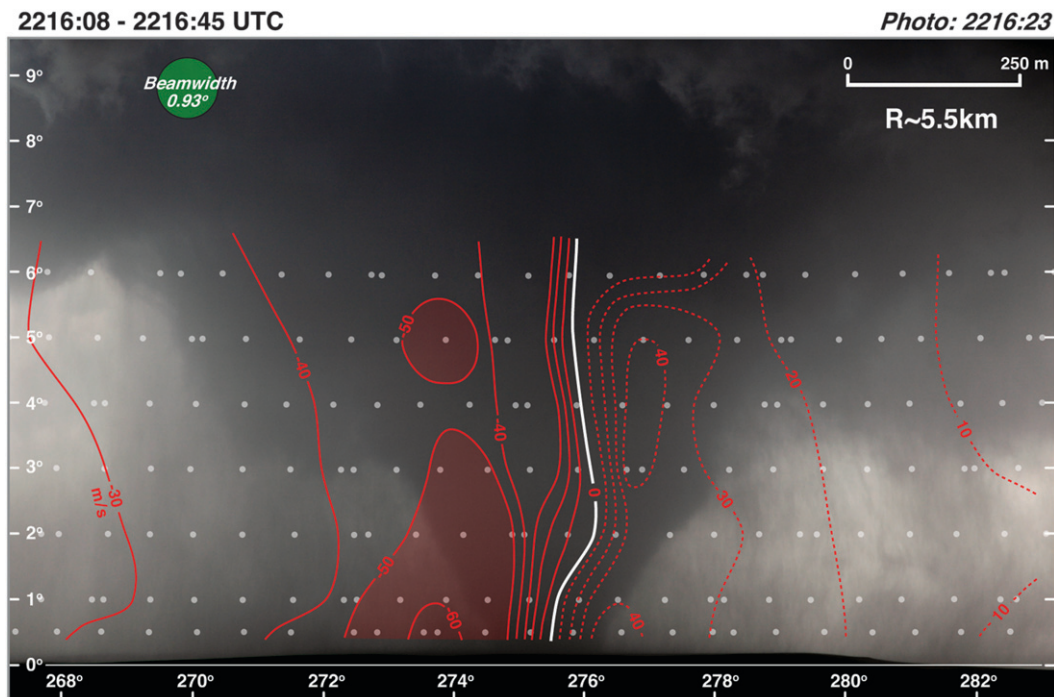


FIG. 4. Photograph of the LaGrange tornado at 2216:23 UTC. Red lines are isopleths of single-Doppler velocity. Solid and dashed lines represent negative and positive radial velocity, respectively. Values less than -50 m s^{-1} are shaded red. The small dots represent the raw data points from DOW7 between 0.5° and 6° . The scale labeled on the figure is valid at the distance of the tornado ($\sim 5.5 \text{ km}$).

were considered too far from DOW7 and the 2218 UTC volume was the last series of scans before the radar re-deployed to another location. The grid spacing in the vertical was 50 m for both times while the spacing in the horizontal was 50 m and 40 m for the 2216 and 2218 UTC volumes, respectively, to take advantage of the higher data resolution as the tornado approached the radar. See Lee and Wurman (2005) for additional information regarding the GBVTD technique applied to a tornadic circulation.

4. Radar deployments and the hook echo

The LaGrange tornado was rated EF2 by the National Weather Service based on a combination of the documented damage, radial velocities recorded by the DOWs, and in situ wind measurements by the Tornado Intercept Vehicle (TIV; Wurman et al. 2007c). The initial deployment of DOW6 and DOW7 on the LaGrange supercell is shown in Fig. 3. The radars were separated by $\sim 15 \text{ km}$ along an approximate north-south highway (the dual-Doppler lobe is indicated by the dashed line). The characteristics of the hook echo starting with the initial intensification of the low-level circulation (tornadogenesis was estimated to occur at $\sim 2152 \text{ UTC}$) until a couple of minutes before

dissipation at $\sim 2230 \text{ UTC}$ are shown. A weak echo hole² (WEH; Fujita 1981) is apparent at the 2204:07 and 2214:07 UTC times and is collocated with the rotational couplet.

5. GBVTD analysis of the LaGrange tornado

a. 2216:08–2216:45 UTC

As noted in section 3, a GBVTD analysis was performed during the 2216:08–2216:45 and 2218:07–2218:42 UTC volumes owing to the proximity of the tornado to DOW7. The elevation- and azimuth-angle grid superimposed onto the photograph taken at 2216:23 UTC is shown in Fig. 4. This figure was also shown in Wakimoto et al. (2011) and includes the location of the raw data points from DOW7 (0.5° , 1° , 2° , 3° , 4° , 5° , and 6° elevation angles) as well as an analysis of the single-Doppler velocities. The data points illustrate the high-resolution radar information that is available for this volume scan. The radius of maximum winds denoting the tornado core at low levels is slightly larger than the visible funnel (Bluestein et al. 2004).

² Qualitatively defined as the area $< 40 \text{ dBZ}$ embedded within the circulation.

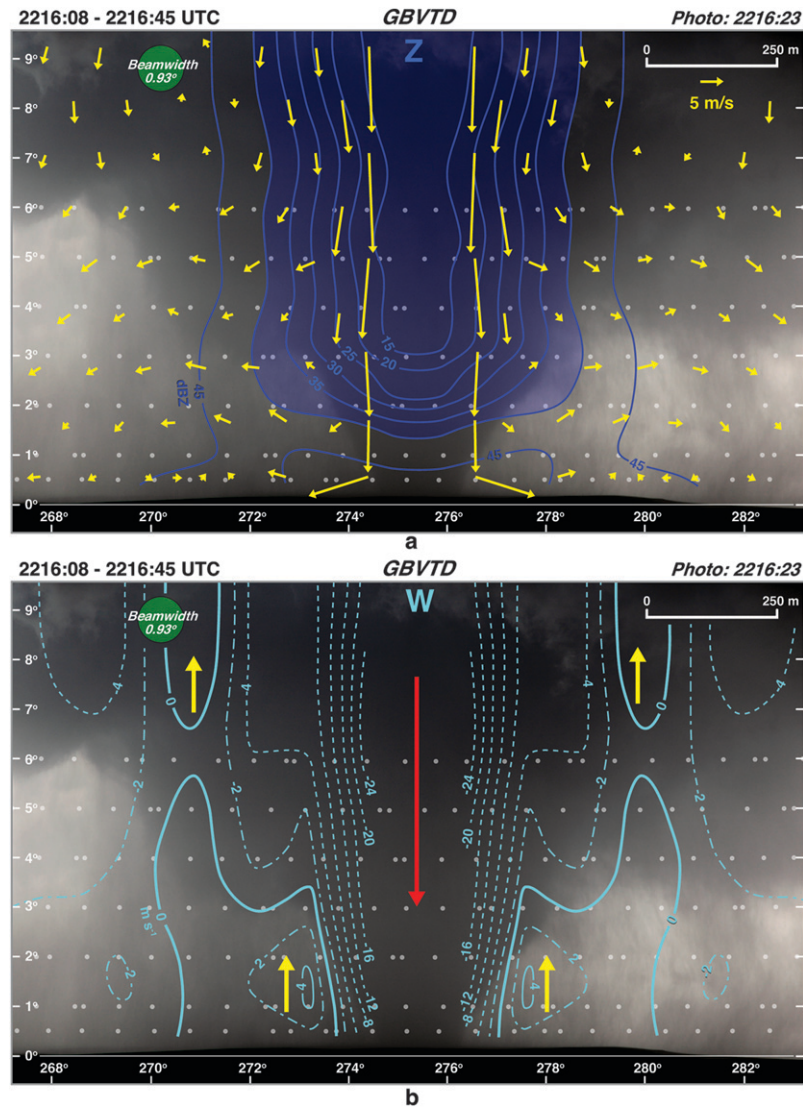


FIG. 5. GBVTD analysis for the 2216:08–2216:45 UTC volume from DOW7 superimposed on top of a photograph of the LaGrange tornado at 2216:23 UTC. (a) Radar reflectivity (dBZ) and the two-dimensional wind field. Reflectivity values less than 40 dBZ are shaded. (b) Vertical velocity (m s^{-1}). Solid and dashed lines represent positive and negative velocities, respectively. Dash-dot contours have been added in regions with weak gradients. Red and yellow arrows denote areas of downdraft and updraft, respectively. (c) Radial velocity (m s^{-1}). Red and blue arrows denote areas of outflow and inflow, respectively. (d) Tangential velocity (m s^{-1}) and the two-dimensional wind field. Solid and dashed lines represent velocities into and out of the figure, respectively. Shaded regions represent magnitudes $>34 \text{ m s}^{-1}$. (e) Perturbation pressure (mb) and the two-dimensional wind field. Shaded region represents perturbation pressure less than -20 mb . (f) Vertical vorticity (10^{-2} s^{-1}) and the two-dimensional wind field. (g) Angular momentum ($10^3 \text{ m}^2 \text{ s}^{-1}$) and the two-dimensional wind field. Shaded regions represent angular momentum greater than $10 \times 10^3 \text{ m}^2 \text{ s}^{-1}$. Dashed isopleths of angular momentum represent an extrapolation of the analysis in a region devoid of data. The small dots represent the raw data points from DOW7 between 0.5° and 6° . The scale labeled on the figure is valid at the distance of the tornado.

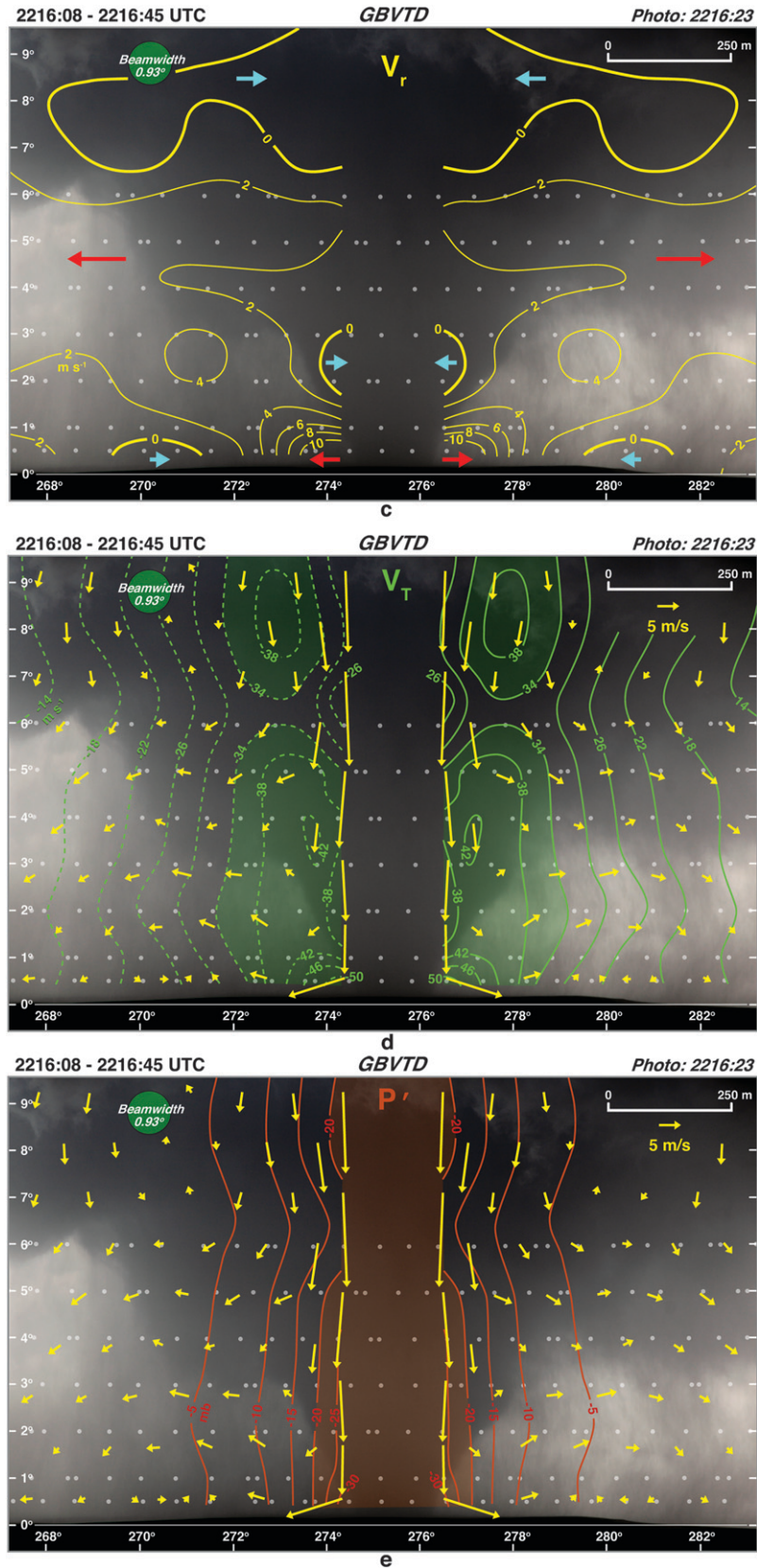


FIG. 5. (Continued)

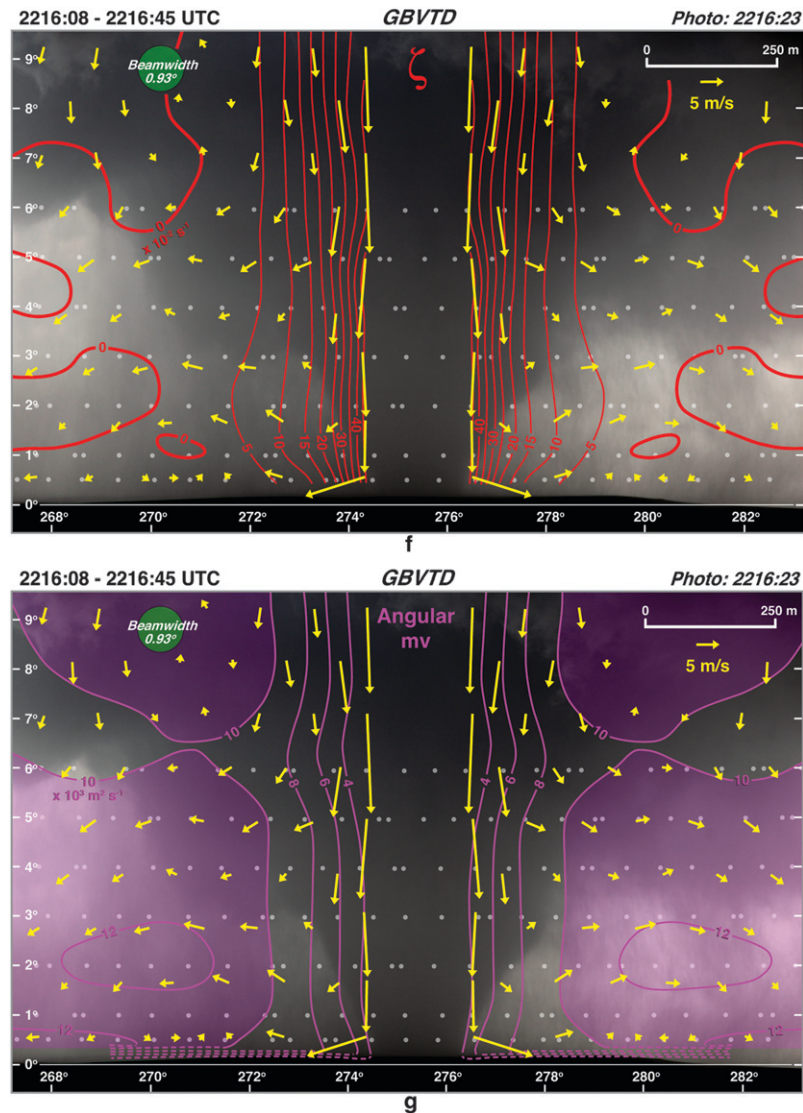


FIG. 5. (Continued)

A vertical cross section of radar reflectivity and the two-dimensional vertical and radial wind field derived from the GBVTD analysis through the center of the tornado is shown in Fig. 5a. The WEH (shaded blue) centered on the tornado resulting from centrifuging of hydrometeors is apparent (Dowell et al. 2005) and is associated with a larger diameter than the visible funnel. The higher reflectivities beneath the WEH at low levels (>45 dBZ) are a result of small debris particles being lofted from the surface (Wakimoto et al. 2011). The prominent feature in the wind field is the axial downdraft (i.e., a downdraft centered along the axis of rotation) that has been noted by other investigators (e.g., Wurman and Gill 2000; Lee and Wurman 2005; Kosiba et al. 2008; Kosiba and Wurman 2010). The GBVTD analysis does not extend to the tornado center owing to the

lack of data points at small radii that are required to perform the Fourier decomposition (Carbone et al. 1985). Accordingly, no analysis is shown for a radius <100 m for this time and <80 m for the volume discussed in section 5b.

The downdraft speeds within the tornado exceed 24 m s^{-1} (Fig. 5b) and are largely confined within the condensation funnel. The isopleths of negative vertical velocity at low levels slope outward with increasing height similar to the shape of the funnel. The maximum of updraft just above the surface (between 1° and 2°) is $>4 \text{ m s}^{-1}$ and is located at the periphery of the funnel, which suggests a two-celled structure (e.g., Davies-Jones 1986). Strong, low-level outflow in mean radial velocities is found near the tornado in response to the axial downdraft (Fig. 5c). Shallow inflow (also seen in Fig. 5a)

is confined to a small region outside of the tornado core. Section 6 presents additional discussion of the low-level inflow.

The mean tangential velocities derived from the GBVTD methodology are presented in Fig. 5d. The maximum speeds are in excess of 50 m s^{-1} near the surface and consistent with the ground-relative, single-Doppler velocities shown in Fig. 4 (the tornado-relative Doppler velocities can be obtained by adding $\sim 12 \text{ m s}^{-1}$, the speed of the tornado toward DOW7, to the field in Fig. 4). The expected frictional decrease in tangential velocities within the surface boundary layer is not being resolved by DOW7. The existence of strong rotation near the ground suggests that a downward-directed perturbation pressure (hereafter, perturbation pressure is referred to as pressure) gradient exists. The pressure field (Fig. 5e) is calculated using the equation outlined by Lee and Wurman (2005). The pressure deficits at each height are obtained independently assuming that all perturbations at 3-km radius are zero (Lee and Wurman 2005). Accordingly, the reader should interpret the vertical pressure gradient with some caution (e.g., Gal-Chen 1978). However, all plots of pressure deficits with radius (not shown) reveal no change in pressure beyond a radius of 1 km. A surface-based mesolow ($< -30 \text{ mb}$) results in a strong vertical gradient of pressure, consistent with the existence of the axial downdraft (also noted by Lee and Wurman 2005). The field presented in Fig. 5e is dominated by the cyclostrophic pressure gradient balancing the primary tornadic circulation. A weaker, advection pressure gradient³ term (not shown) supports the secondary circulation. The reduction in pressure extends beyond the visible funnel, but is limited to an approximate radius of 300–400 m from the tornado center.

The maximum vertical vorticity values are $>45 \times 10^{-2} \text{ s}^{-1}$ within the tornado core⁴ (Fig. 5f). A strong radial gradient results in values rapidly approaching 0 outside of the tornado funnel. Indeed, the low-level vorticity is relatively weak approximately one funnel-width beyond the visible edge of the condensation funnel. The distribution of the angular momentum fields near tornadoes has been documented by Lee and Wurman (2005),

Rasmussen and Straka (2007), Kosiba et al. (2008), and Kosiba and Wurman (2010). It has been noted that the angular momentum is relatively constant with height near and within the radius of maximum wind (Lee and Wurman 2005; Kosiba et al. 2008; Kosiba and Wurman 2010) and is similar to the axisymmetric profiles associated with hurricanes (e.g., Lee et al. 2000). In addition, high-resolution simulations of tornadoes produce nearly vertical isopleths of angular momentum (e.g., Lewellen et al. 2000). Figure 5g is consistent with these past studies with approximate upright isopleths near the tornado. The angular momentum increases radially outward with the strongest gradient within and just beyond the visible funnel. Low angular momentum flow that should exist near the surface is not being detected by the Doppler radar but is represented by the dashed isopleths plotted at low levels. The wind field presented in Fig. 5g depicts strong surface outflow near the tornado but also generally weaker outflow throughout the region. Accordingly, angular momentum is being advected away from the tornado and it would be expected that the LaGrange tornado will weaken with time [this observation is consistent with the results shown by Atkins et al. (2012)]. This possible trend will be assessed in the next session.

b. 2218:07–2218:42 UTC

The axial downdraft increased in intensity aloft ($< -32 \text{ m s}^{-1}$) during the 2218:07–2218:42 UTC volume scan but is weaker at low levels (Figs. 6a,b). The strong downdrafts aloft can be partially attributed to the ability to resolve the wind field closer to the center of the tornado as the circulation approached the DOW7 site. Low-level updrafts are still confined to the periphery of the visible funnel (Fig. 6b), but are weaker than the velocities shown in the previous analysis time (Fig. 5b). The strength and radial extent of the inflow near the surface increased (Figs. 6a,c). Radial outflow above the boundary layer inflow is clearly apparent (maximum value $>6 \text{ m s}^{-1}$ at $\sim 250 \text{ m}$ above the ground along the edges of the condensation funnel). This type of flow is consistent with the presence of a secondary circulation and has also been shown in Lee and Wurman (2005), Kosiba et al. (2008), and Kosiba and Wurman (2010). The reader should view the increased intensity and extent of the inflow near the surface with caution since it is possible that the approaching tornado allowed for Doppler velocities to be collected closer to the ground during this time owing to the smaller beamwidth and lower height of the center of the beam axis. Vertical velocities surrounding tornadoes derived from the GBVTD technique should also be viewed with caution since the divergence fields at the lower boundary may not be fully resolved.

³ Lee and Wurman (2005) define the radial pressure gradient equation (excluding the Coriolis and friction terms). They partition the pressure gradient into the contributions by the cyclostrophic and advection pressure gradients.

⁴ Single-Doppler estimates of the horizontal shear suggest that the maximum vertical vorticity was approximately $160 \times 10^{-2} \text{ s}^{-1}$ (Wakimoto et al. 2011). The larger estimate of vorticity resulted from the higher resolution of the single-Doppler velocity data and the inability of the GBVTD analysis to resolve the vertical vorticity close to the tornado center.

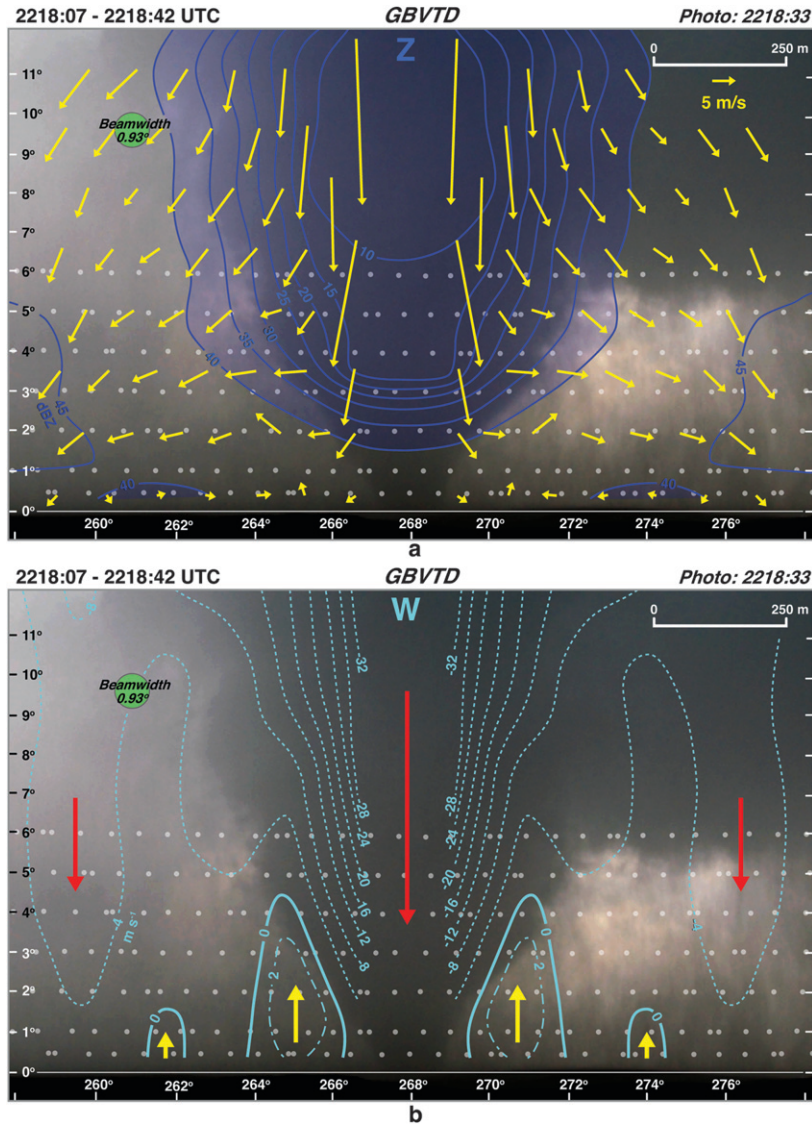


FIG. 6. GBVTD analysis for the 2218:07–2218:42 UTC volume from DOW7 superimposed on top of a photograph of the LaGrange tornado at 2218:33 UTC. (a) Radar reflectivity (dBZ) and the two-dimensional wind field. Reflectivity values less than 40 dBZ are shaded. (b) Vertical velocity (m s^{-1}). Solid and dashed lines represent positive and negative velocities, respectively. Dash-dot contours have been added in regions with weak gradients. Red and yellow arrows denote areas of downdraft and updraft, respectively. (c) Radial velocity (m s^{-1}). Solid and dashed lines represent positive and negative velocities, respectively. Red and blue arrows denote areas of outflow and inflow, respectively. (d) Tangential velocity (m s^{-1}) and the two-dimensional wind field. Solid and dashed lines represent velocities into and out of the figure, respectively. Shaded regions represent magnitudes $>34 \text{ m s}^{-1}$. (e) Perturbation pressure (mb) and the two-dimensional wind field. Shaded region represents perturbation pressure less than -20 mb . (f) Vertical vorticity (10^{-2} s^{-1}) and the two-dimensional wind field. Representative vertical vorticity isopleths from the 2216:08–2216:45 UTC volume are plotted (light blue dotted lines). (g) Angular momentum ($10^3 \text{ m}^2 \text{ s}^{-1}$) and the two-dimensional wind field. Shaded regions represent angular momentum greater than $10 \times 10^3 \text{ m}^2 \text{ s}^{-1}$. Dashed isopleths of angular momentum represent an extrapolation of the analysis in a region devoid of data. Representative angular momentum isopleths from the 2216:08–2216:45 UTC volume are plotted (light blue dotted lines). The small dots represent the raw data points from DOW7 between 0.5° and 6° . The scale labeled on the figure is valid at the distance of the tornado.

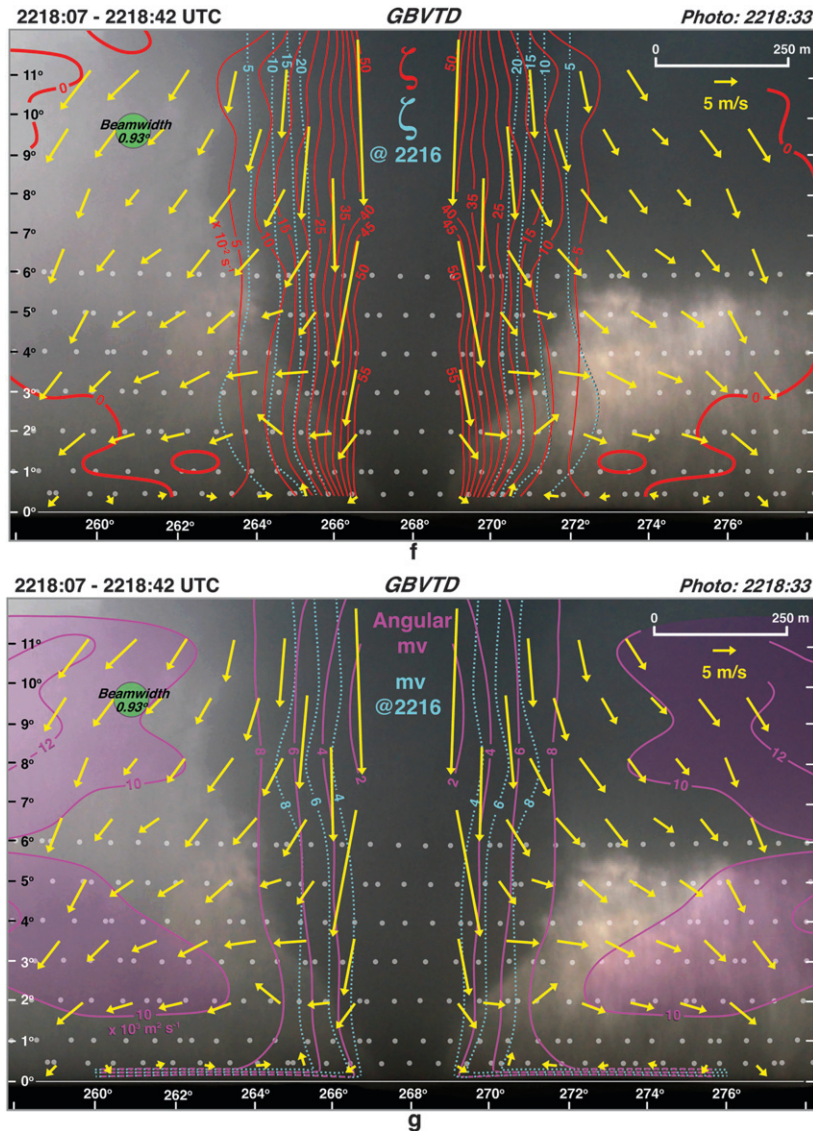


FIG. 6. (Continued)

The diffused flow field depicting angular momentum being advected out from the tornado during the previous analysis time (Fig. 5g) suggests that the circulation might be weakening. Indeed, the tangential velocities have decreased at all levels (Fig. 6d). A time plot of azimuthal shear based on the raw single-Doppler velocities from DOW7 (Fig. 7) also shows a decrease in intensity at this time. The weaker rotational speeds result in a higher minimum pressure within the surface mesolow (Fig. 6e) and a weaker downward-directed pressure gradient. Interestingly, the peak vertical vorticity has increased and is now $>55 \times 10^{-2} \text{ s}^{-1}$ (Fig. 6f). This increase is a result of the GBVTD analysis resolving larger vorticity values closer to the center of the circulation than the previous analysis time. Single-Doppler velocity data

(not shown) reveal that the tornado circulation is contracting at this time. The contraction of the circulation in a diffused wind field at low levels appears to be contradictory; however, it is believed that centrifuging of hydrometeors is masking low-level confluent wind field into the tornado. This possibility is explored in the next section.

An alternative way to assess the overall trend in vertical vorticity is to compare the values observed at 2216:08–2216:45 UTC with the current analysis time. A few isopleths (light blue dashed lines) from the earlier time are plotted near the periphery of the funnel. This comparison illustrates that the vertical vorticity has increased slightly at most heights. This increase appears to be inconsistent with the observed weakening of the

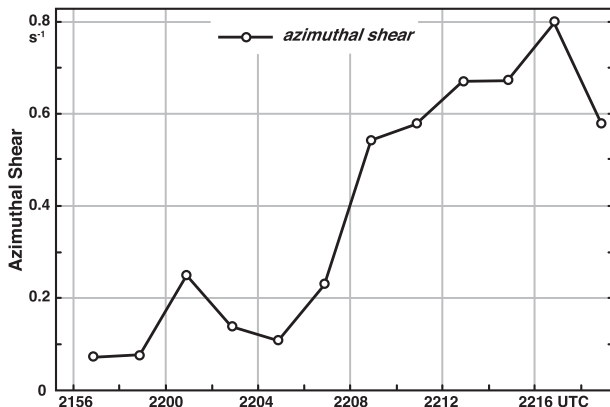


FIG. 7. Time plot of azimuthal shear associated with the tornado based on single-Doppler velocity measurements at 0.5° from DOW7.

tangential velocities and azimuthal shear at this analysis time. An examination of the components that contribute to vertical vorticity reveals that this increase was attributable to an increase in the shear vorticity even though the curvature vorticity weakens. A similar comparison with the angular momentum fields (Fig. 6g), however, shows that there is an overall decrease in angular momentum within the tornado core compared with the early volume. The diffluent pattern in the wind field is more pronounced compared to the earlier time and continues to support angular momentum being advected away from the tornado (also shown by Rasmussen and Straka 2007). As previously mentioned, the LaGrange tornado dissipated at ~ 2230 UTC.

6. Low-level convergence and the centrifuging of hydrometeors

Mobile Doppler radars have collected unprecedented high-resolution data of tornadoes. However, it has been difficult to collect information at the lowest tens of meters where the strongest radial inflow would be expected (e.g., Lewellen et al. 1997). In addition, centrifuging of hydrometeors/debris within the tornado could be masking the convergence signal at low levels (e.g., Wurman and Gill 2000; Dowell et al. 2005). The impact of centrifuging of hydrometeors is schematically illustrated in Fig. 8. The path of the hydrometeors is different than air parcels since there is a net outward trajectory of the particles (Dowell et al. 2005). This centrifuging contributes to the formation of the WEH and biases the Doppler velocities with a false divergent signature (i.e., a positive bias to the radial velocity measurements).

Past investigations have provided estimates of this centrifuging effect and suggested that it could be important (Wurman and Gill 2000; Dowell et al. 2005). Lee and Wurman (2005) suggest that the large radius of

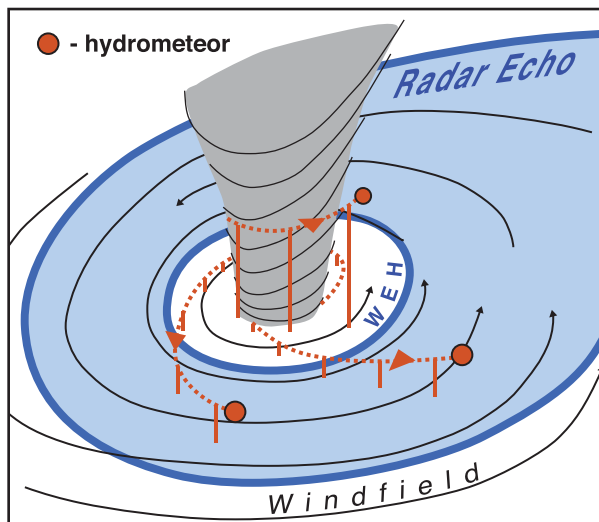


FIG. 8. Schematic illustrating the centrifuging of hydrometeors within and near an intense tornadic circulation. Centrifuging leads to the creation of a WEH, which was larger than the funnel cloud in the current case. The figure also illustrates the difference between the wind field (black lines) and the trajectory of the hydrometeors (orange dashed lines). The latter is measured by a Doppler radar and leads to a positive bias in the derived radial velocities accompanying the tornado.

maximum wind and strong radial inflow for the Mulhall tornado would have largely negated the impact of centrifuging and resulted in a “minor shift of the overall pattern,” but would not have altered the general conclusions of their study. Rasmussen and Straka (2007) did not incorporate Doppler velocity data close to the center of the tornado when calculating angular momentum owing to a concern that centrifuging of debris would contaminate estimates of the radial velocity. The LaGrange tornado was not violent (EF2) and was characterized by relatively weak radial inflow and small radius of maximum wind. As a result, the two-dimensional wind profile associated with this type of tornado could be strongly influenced by the centrifuging of hydrometeors.

The technique to estimate the effect of centrifuging used in this study follows the approach outlined by Dowell et al. (2005). They developed equations governing the motion of particles/objects for a steady, axisymmetric tornado neglecting subgrid-scale processes such as coalescence of hydrometeors. The particle's/object's drag coefficient is assumed constant and equal to the value attained when the object is falling at its terminal velocity. In addition, the hydrometeor's and other objects' impact on the airflow are also ignored (e.g., Eskridge and Das 1976). The type and size distribution of the radar scatterers were not known since polarimetric observations that were collected on the LaGrange tornado were not suitable for use in this study. These types of

measurements have proven particularly useful in discriminating between particle types (e.g., Ryzhkov et al. 2005; Bluestein et al. 2007b). High-definition video and a few observations from personnel deployed near the tornado did not suggest lofting of large debris particles. The higher echo return at low levels was likely a combination of precipitation, small twigs, dirt/gravel, and wet grass that had become airborne in the circulation.

To simplify the estimates of centrifuging presented in this paper, the effect of small debris particles was ignored and it was assumed that radar reflectivity returns were exclusively from hydrometeors. In lieu of a known drop size distribution, the median volume diameter (D_o) was calculated from the radar reflectivity profile based on a Marshall–Palmer size distribution (Marshall and Palmer 1948). It was assumed that D_o represents the drop size in the radar sampling volume. The uncertainty in the DOW7 radar reflectivity values stated in section 2 would translate to an uncertainty of $\sim \pm 0.1$ mm in D_o at 40 dBZ. The terminal velocity can be estimated based on the known drop size (Atlas et al. 1973). The drops were assumed to initially move with the same horizontal mean GBVTD velocities as the air. Subsequently, the particle motions are determined by the forcing rather than by the initialization. The results presented in Figs. 9, 10, and 11 are after sufficient time had elapsed such that the particle motion has asymptotically approached the steady solutions. The impact of particle motion was negligible on the GBVTD mean tangential velocities, vertical vorticity, and angular momentum plots (not shown). The reader is referred to Dowell et al. (2005) for additional information concerning the particle motion calculations.

The estimated positive bias to the radial velocities for 2216:08–2216:45 and 2218:07–2218:42 UTC are plotted in Figs. 9a,b, respectively. The effect of centrifuging of hydrometeors is similar for both analysis times. Not surprisingly, the largest impact is at low levels where the tangential velocities are the strongest and are also close to the center of the tornado. The same conclusion was reached in a sensitivity study where a uniform radar reflectivity profile was substituted for the actual echo values (Figs. 5a and 6a) and the particle motion calculations were repeated. The centrifuging effect decreases rapidly and is small (~ 1 m s⁻¹) at distances greater than a few hundred meters from the core axis. The particle radial velocities depicted in Fig. 9 are of the same order of magnitude as the radial velocities from the wind shown in Figs. 5c and 6c and would significantly impact the divergence fields, especially at low levels. The measured radial velocity profiles were corrected for the particle motions shown in Fig. 9 by subtracting the two fields, after which a new divergence analysis was created (not

shown). The modified vertical velocity field (Figs. 10 and 11) reveals striking differences with the plots shown in Figs. 5b and 6b. The axial downdraft extending throughout the tornadic circulation at 2216:08–2216:45 UTC is absent (Figs. 10a and 11a). Downdrafts (< -4 m s⁻¹) are confined to the lowest few hundred meters while positive vertical motions exist (> 8 m s⁻¹) at higher levels. The strong radial outflow near the surface (Figs. 5a,c) has been reduced. The corrected wind field near the tornado at 2218:07–2218:42 UTC is also different than the early time. Low-level updrafts within the tornado core are apparent and are supported by stronger radial inflow near the surface (Figs. 10b and 11b). Weak axial downdrafts exist aloft.

The estimate of the centrifuging of hydrometeors should be viewed with caution and is subject to the assumptions used in the calculation stated earlier in this section. However, these results suggest that Doppler radar data collected on tornadoes associated with a small radius of maximum wind and relatively weaker inflow could be significantly biased owing to particle centrifuging such that the radial and vertical velocity wind field near and within the tornado core is significantly altered. Indeed, the prominent axial downdraft shown in the present case was reduced owing to the increased low-level convergence into the core after a correction was applied.

The ability to capture the low-level inflow into tornadoes remains a challenge. Resolving this component of the wind is critical since it sets the lower boundary condition for the vertical velocity calculations. There are two interpretations for the increase in the low-level radial inflow near the tornado with time (Figs. 5c and 6c). It is possible that the differences are a result of the natural tornado evolution. However, it is also possible that the increase in magnitude and areal extent of the inflow is a result of the radar's ability to better resolve the low-level flow as the tornado approached. The authors have concluded that the latter is the more likely scenario since the areal coverage of the radar beamwidth, at the distance of the tornado, decreases by more than 50% when comparing the 2216 and 2218 UTC analysis times. This increase in spatial resolution results in finescale Doppler velocity measurements at low levels. Therefore, we recommend that the radar be deployed within a few kilometers of the tornado or that other high-resolution (narrow beamwidth) observing platforms be used such as a W- or K-band radar (e.g., Bluestein et al. 2007a) or a lidar (e.g., Bluestein et al. 2010). Figure 12 attempts to summarize the difficulty of accurately measuring the low-level inflow into the tornado owing to the centrifuging of hydrometeors and debris and the inability of the radar beam to fully resolve the inflow, which is confined to the lowest levels.

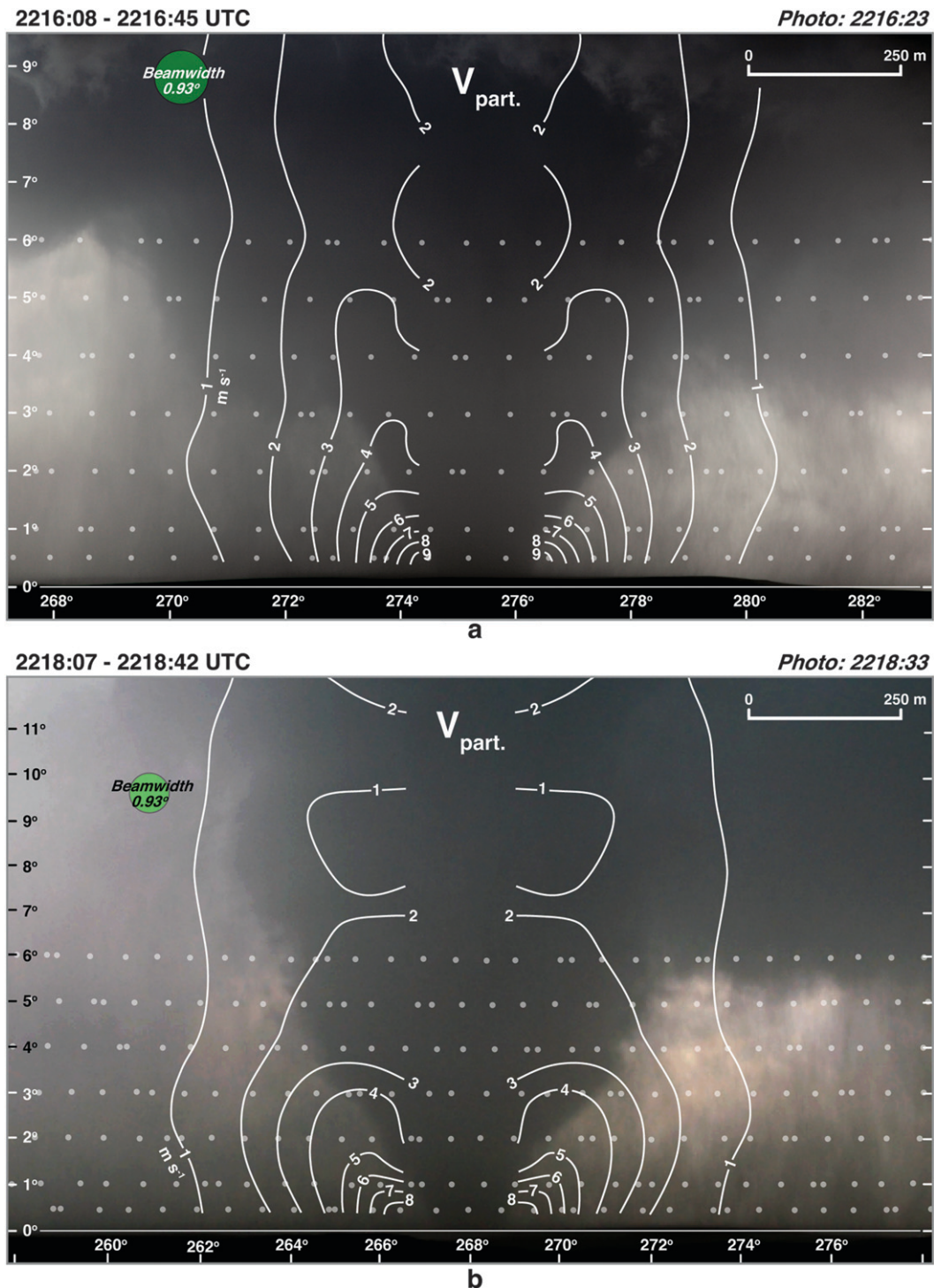


FIG. 9. Estimate of the positive bias to the radial velocity profile owing to the centrifuging of hydrometeors for (a) 2216:08–2216:45 and (b) 2218:07–2218:42 UTC.

7. Summary and discussion

The current study presents a GBVTD radar analysis combined with cloud photography of the LaGrange,

Wyoming, tornado on 5 June 2009 during VORTEX2. The funnel was within a few kilometers of the Doppler radar resulting in a dataset that could be used to reconstruct the three-dimensional wind field associated

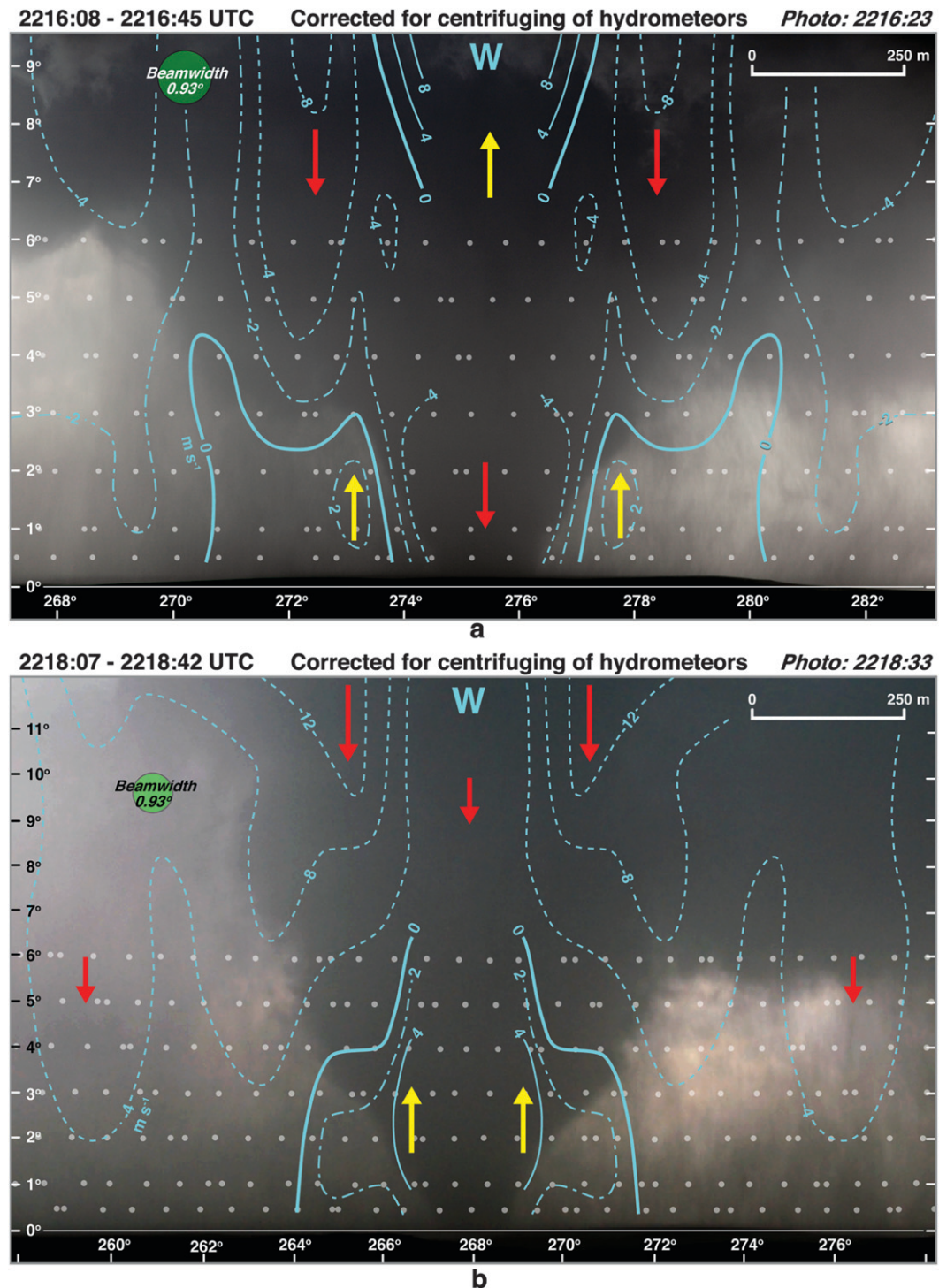


FIG. 10. Estimate of the vertical velocities after removing the effect of centrifuging of hydrometeors for (a) 2216:08–2216:45 and (b) 2218:07–2218:42 UTC. Solid and dashed lines represent positive and negative velocities, respectively. Dash-dot contours have been added in regions with weak gradients. Red and yellow arrows denote areas of downdraft and updraft, respectively.

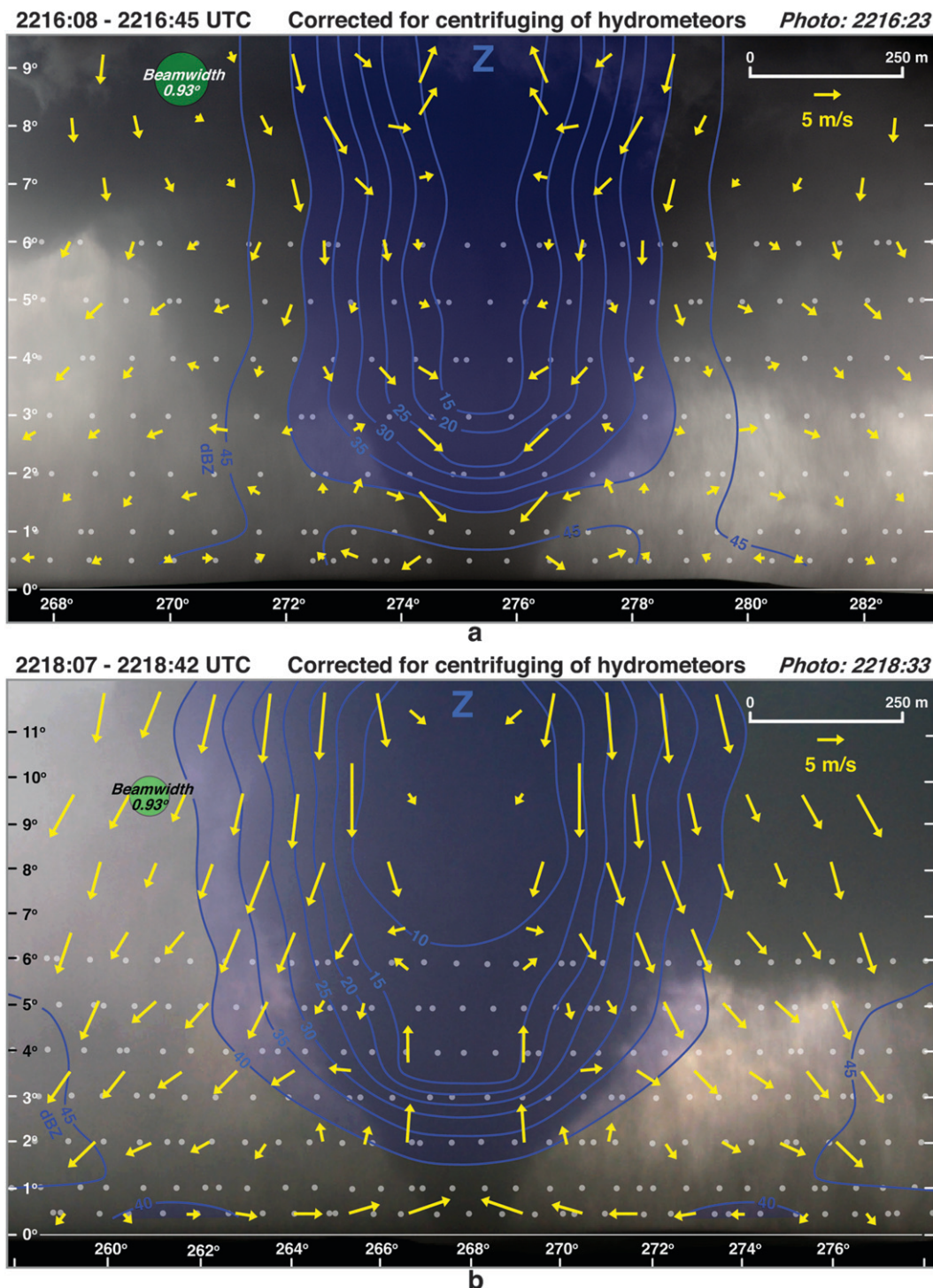


FIG. 11. Radar reflectivity and an estimate of the two-dimensional wind field after removing the effect of centrifuging of hydrometeors for (a) 2216:08–2216:45 and (b) 2218:07–2218:42 UTC. Radar reflectivities shaded blue are less than 40 dBZ.

with the tornadic circulation. A strong axial downdraft was evident and was supported by a downward-directed pressure gradient. Weak radial inflow at low levels was apparent. The weak inflow was attributed to a combination

of centrifuging of hydrometeors/debris in the tornado associated with a small radius of maximum wind and the inability of the radar beam to fully resolve the low-level flow. The mean tangential winds exceeded 50 m s^{-1}

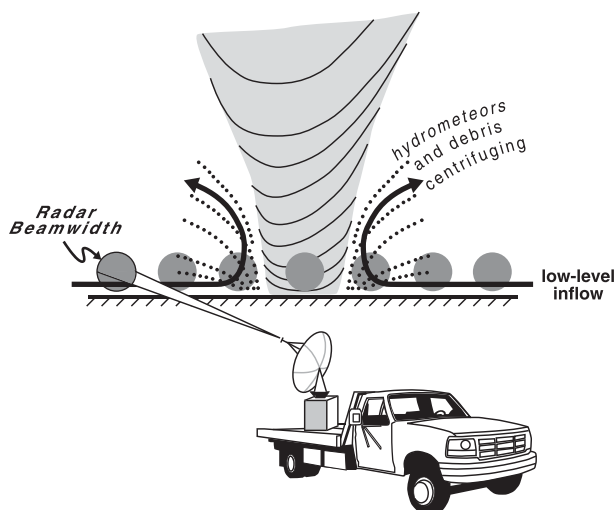


FIG. 12. Schematic illustrating the difficulty in measuring the low-level inflow into tornadoes. Centrifuging of hydrometeors and debris results in a positive bias in the radial velocities. In addition, the challenge of scanning near the ground is shown by the inability of the radar beam to fully resolve the low-level radial inflow.

and were located near the surface. The tornado was accompanied by an intense column of vertical vorticity that rapidly weakened approximately one funnel width beyond the visible edge of the funnel cloud. Angular momentum was advected away from the circulation, consistent with the observed weakening of the tornado during the analysis period.

The availability of a dual-Doppler wind synthesis provided an opportunity to assess the assumptions used in the GBVTD methodology. The analysis suggests that the presence of weak radial inflow requires one of the higher-order terms that has been traditionally ignored in past GBVTD analyses be retained in order to retrieve the most accurate wind field. In addition, a quantitative analysis of the centrifuging of hydrometeors suggests that the radial and vertical velocity profile near and within the tornado can be significantly altered for intense circulations accompanied by a small radius of maximum wind and relatively weak low-level inflow. Indeed, the intense axial downdraft within the tornado was largely absent when an attempt to correct for hydrometeor centrifuging was applied. The latter conclusion is subject to the assumptions used in estimating the centrifuging effect. The effect of particle motion on the mean tangential velocities, vertical vorticity, and angular momentum was negligible.

The analysis of the LaGrange tornado highlights the difficulty of achieving high-resolution dual-Doppler wind synthesis of tornadic wind fields. Techniques such as the GBVTD will need to be applied along with remote

sensing techniques that are better able to resolve the low-level inflow into the tornado. Polarimetric data will also be important to assess the hydrometeor type and the location of debris in removing possible contamination of the Doppler velocity data. Future studies will, hopefully, be able to apply the techniques illustrated in this paper on tornadoes of different intensity and widths and also for a longer period of the tornado's life cycle. These additional analyses will also be needed to verify the results shown in this paper, which were restricted to two radar volume scans.

Acknowledgments. Any opinion, findings, conclusions, or recommendations expressed in this publication are those of the authors and do not necessarily reflect the views of the National Science Foundation. The authors wish to thank David Dowell who provided several helpful suggestions for calculating the particle motion. Research results presented in this paper were supported by the National Science Foundation under Grant ATM-0757714. The DOW radars are National Science Foundation Lower Atmospheric Observing Facilities supported by Grant ATM-0734001. The DOW deployments in VORTEX2 have been supported by Grants ATM-0910737 and ATM-0966095. Analysis of DOW data has been supported by Grant ATM-0947235. VORTEX2 has been supported, in part, by Grant ATM-0724318. Comments by three anonymous reviewers significantly improved an earlier version of this manuscript.

REFERENCES

- Abrams, T., 1952: *The Manual of Photogrammetry*. George Banta Publishing, 876 pp.
- Alexander, C. R., and J. Wurman, 2005: The 30 May 1998 Spencer, South Dakota, storm. Part I: The structural evolution and environment of the tornadoes. *Mon. Wea. Rev.*, **133**, 72–96.
- Atkins, N. T., A. McGee, R. Ducharme, R. M. Wakimoto, and J. Wurman, 2012: The LaGrange tornado during VORTEX2. Part II: Photogrammetric analysis of the tornado combined with dual-Doppler radar data. *Mon. Wea. Rev.*, **140**, 2939–2958.
- Atlas, D., R. C. Srivastava, and R. S. Sekhon, 1973: Doppler radar characteristics of precipitation at vertical incidence. *Rev. Geophys. Space Phys.*, **2**, 1–35.
- Bluestein, H. B., 1999: A history of severe-storm-intercept field programs. *Wea. Forecasting*, **14**, 558–577.
- , J. G. LaDue, H. Stein, D. Speheger, and W. P. Unruh, 1993: Doppler radar wind spectra of supercell tornadoes. *Mon. Wea. Rev.*, **121**, 2200–2221.
- , W. P. Unruh, D. C. Dowell, T. A. Hutchinson, T. M. Crawford, A. C. Wood, and H. Stein, 1997: Doppler radar analysis of the Northfield, Texas, tornado of 25 May 1994. *Mon. Wea. Rev.*, **125**, 212–230.
- , W.-C. Lee, M. Bell, C. C. Weiss, and A. L. Pazmany, 2003: Mobile Doppler radar observations of a tornado in a supercell near Bassett, Nebraska, on 5 June 1999. Part II: Tornado-vortex structure. *Mon. Wea. Rev.*, **131**, 2968–2984.

- , C. C. Weiss, and A. L. Pazmany, 2004: The vertical structure of a tornado near Happy, Texas, on 5 May 2002: High-resolution, mobile, W-band, Doppler radar observations. *Mon. Wea. Rev.*, **132**, 2325–2337.
- , —, M. M. French, E. M. Holthaus, R. L. Tanamachi, S. Frasier, and A. L. Pazmany, 2007a: The structure of tornadoes near Attica, Kansas, on 12 May 2004: High-resolution, mobile, Doppler radar observations. *Mon. Wea. Rev.*, **135**, 475–506.
- , M. M. French, R. L. Tanamachi, S. Frazier, K. Hardwick, F. Junyent, and A. L. Pazmany, 2007b: Close range observations of tornadoes in supercells made with a dual-polarization, X-band, mobile Doppler radar. *Mon. Wea. Rev.*, **135**, 1522–1543.
- , and Coauthors, 2010: A summary of data collected during VORTEX2 by MWR-05XP/TWOLF, UMASS X-pol, and the UMASS W-band radar. Preprints, *25th Conf. on Severe Local Storms*, Denver, CO, Amer. Meteor. Soc., P5.4. [Available online at <https://ams.confex.com/ams/pdfpapers/176197.pdf>.]
- Brown, R. A., L. R. Lemon, and D. W. Burgess, 1978: Tornado detection by pulsed Doppler radar. *Mon. Wea. Rev.*, **106**, 29–38.
- Browning, K. A., and R. Wexler, 1968: The determination of kinematic properties of a wind field using Doppler radar. *J. Appl. Meteor.*, **7**, 105–113.
- Burgess, D. W., M. A. Magsig, J. Wurman, D. C. Dowell, and Y. Richardson, 2002: Radar observations of the 3 May 1999 Oklahoma City tornado. *Wea. Forecasting*, **17**, 456–471.
- Carbone, R. E., M. J. Carpenter, and C. D. Burghart, 1985: Doppler radar sampling limitations in convective storms. *J. Atmos. Oceanic Technol.*, **2**, 357–361.
- Davies-Jones, R. P., 1986: Tornado dynamics. *Thunderstorms: A Social, Scientific and Technological Documentary*, Vol. 2, *Thunderstorm Morphology and Dynamics*, E. Kessler, Ed., University of Oklahoma Press, 197–236.
- Dowell, D. C., C. R. Alexander, J. M. Wurman, and L. J. Wicker, 2005: Centrifuging of hydrometeors and debris in tornadoes: Radar reflectivity patterns and wind-measurement errors. *Mon. Wea. Rev.*, **133**, 1501–1524.
- Eskridge, R. E., and P. Das, 1976: Effect of a precipitation-driven downdraft on a rotating wind field: A possible trigger mechanism for tornadoes? *J. Atmos. Sci.*, **33**, 70–84.
- Forbes, G. S., 1981: On the reliability of hook echoes as tornado indicators. *Mon. Wea. Rev.*, **109**, 1457–1466.
- Fujita, T. T., 1981: Tornadoes and downbursts in the context of generalized planetary scales. *J. Atmos. Sci.*, **38**, 1511–1534.
- Gal-Chen, T., 1978: A method for the initialization of the anelastic equations for matching models with observations. *Mon. Wea. Rev.*, **106**, 587–606.
- Holle, R. L., 1986: Photogrammetry of thunderstorms. *Thunderstorms: A Social and Technological Documentary*, Vol. 3, *Thunderstorm Morphology and Dynamics*, E. Kessler, Ed., University of Oklahoma Press, 77–98.
- Koch, S. E., M. desJardins, and P. J. Kocin, 1983: An interactive Barnes objective map analysis scheme for use with satellite and conventional data. *J. Climate Appl. Meteor.*, **22**, 1487–1503.
- Kosiba, K., and J. Wurman, 2010: The three-dimensional axisymmetric wind field structure of the Spencer, South Dakota, 1998 tornado. *J. Atmos. Sci.*, **67**, 3074–3083.
- , R. J. Trapp, and J. Wurman, 2008: An analysis of the axisymmetric three-dimensional low level wind field in a tornado using mobile radar observations. *Geophys. Res. Lett.*, **35**, L05805, doi:10.1029/2007GL031851.
- Lee, W.-C., and F. D. Marks, 2000: Tropical cyclone kinematic structure retrieved from single Doppler radar observations. Part II: The GBVTD-simplex center finding algorithm. *Mon. Wea. Rev.*, **128**, 1925–1936.
- , and J. Wurman, 2005: Diagnosed three-dimensional axisymmetric structure of the Mulhall tornado on 3 May 1999. *J. Atmos. Sci.*, **62**, 2373–2393.
- , F. D. Marks, and R. E. Carbone, 1994: Velocity track display—A technique to extract real-time tropical cyclone circulations using a single airborne Doppler radar. *J. Atmos. Oceanic Technol.*, **11**, 337–356.
- , B. J.-D. Jou, P.-L. Chang, and S.-M. Deng, 1999: Tropical cyclone kinematic structure retrieved from single-Doppler radar observations. Part I: Interpretation of Doppler velocity patterns and the GBVTD technique. *Mon. Wea. Rev.*, **127**, 2419–2439.
- , —, —, and F. D. Marks, 2000: Tropical cyclone kinematic structure retrieved from single-Doppler radar observations. Part III: Evolution and structure of Typhoon Alex (1987). *Mon. Wea. Rev.*, **128**, 3982–4001.
- Lewellen, D. C., and W. S. Lewellen, 2007a: Near surface intensification of tornado vortices. *J. Atmos. Sci.*, **64**, 2176–2194.
- , and —, 2007b: Near-surface vortex intensification through corner flow collapse. *J. Atmos. Sci.*, **64**, 2195–2209.
- , —, and J. Xia, 2000: The influence of a local swirl ratio on tornado intensification near the surface. *J. Atmos. Sci.*, **57**, 527–544.
- Lewellen, W. S., D. C. Lewellen, and R. I. Sykes, 1997: Large eddy simulation of a tornado's interaction with the surface. *J. Atmos. Sci.*, **54**, 581–605.
- Majcen, M., P. Markowski, Y. Richardson, D. Dowell, and J. Wurman, 2008: Multipass objective analyses of Doppler radar data. *J. Atmos. Oceanic Technol.*, **25**, 1845–1858.
- Malkus, J., 1952: The slopes of cumulus clouds in relation to external wind shear. *Quart. J. Roy. Meteor. Soc.*, **78**, 530–542.
- Marquis, J., Y. Richardson, J. Wurman, and P. Markowski, 2008: Single- and dual-Doppler analysis of a tornadic vortex and surrounding storm-scale flow in the Crowell, Texas, supercell of 30 April 2000. *Mon. Wea. Rev.*, **136**, 5017–5043.
- Marshall, J. S., and W. Palmer, 1948: The distribution of raindrops with size. *J. Meteor.*, **5**, 165–166.
- Oye, R., C. Mueller, and S. Smith, 1995: Software for radar translation, visualization, editing, and interpolation. Preprints, *27th Conf. on Radar Meteorology*, Vail, CO, Amer. Meteor. Soc., 359–361.
- Pauley, P. M., and X. Wu, 1990: The theoretical, discrete, and actual response of the Barnes objective analysis scheme for one- and two-dimensional fields. *Mon. Wea. Rev.*, **118**, 1145–1163.
- Rasmussen, E. N., and J. M. Straka, 2007: Evolution of low-level angular momentum in the 2 June 1995 Dimmitt, Texas, tornado cyclone. *J. Atmos. Sci.*, **64**, 1365–1378.
- , R. Davies-Jones, and R. L. Holle, 2003: Terrestrial photogrammetry of weather images acquired in uncontrolled circumstances. *J. Atmos. Oceanic Technol.*, **20**, 1790–1803.
- Ryzhkov, A. V., T. J. Schuur, D. W. Burgess, and D. S. Zrnic, 2005: Polarimetric tornado detection. *J. Appl. Meteor.*, **44**, 557–570.
- Snow, J. T., 1984: On the formation of particle sheaths in columnar vortices. *J. Atmos. Sci.*, **41**, 2477–2491.
- Stout, G. E., and F. A. Huff, 1953: Radar records Illinois tornado genesis. *Bull. Amer. Meteor. Soc.*, **34**, 281–284.
- Tanamachi, R. L., H. B. Bluestein, W.-C. Lee, M. Bell, and A. Pazmany, 2007: Ground-based velocity track display

- (GBVTD) analysis of W-band Doppler radar data in a tornado near Stockton, Kansas, on 15 May 1999. *Mon. Wea. Rev.*, **135**, 783–800.
- Wakimoto, R. M., and B. E. Martner, 1992: Observations of a Colorado tornado. Part II: Combined photogrammetric and Doppler radar analysis. *Mon. Wea. Rev.*, **120**, 522–543.
- , H. V. Murphey, D. C. Dowell, and H. B. Bluestein, 2003: The Kellerville tornado during VORTEX: Damage survey and Doppler radar analyses. *Mon. Wea. Rev.*, **131**, 2197–2221.
- , N. T. Atkins, and J. Wurman, 2011: The LaGrange tornado during VORTEX2. Part I: Photogrammetric analysis of the tornado combined with single-Doppler radar data. *Mon. Wea. Rev.*, **139**, 2233–2258.
- Wurman, J., 2001: The DOW mobile multiple-Doppler network. Preprints, *30th Int. Conf. on Radar Meteorology*, Munich, Germany, Amer. Meteor. Soc., P3.3. [Available online at https://ams.confex.com/ams/30radar/techprogram/paper_21572.htm.]
- , and S. Gill, 2000: Finescale radar observations of the Dimmitt, Texas (2 June 1995), tornado. *Mon. Wea. Rev.*, **128**, 2135–2164.
- , J. M. Straka, and E. N. Rasmussen, 1996: Fine-scale Doppler radar observations of tornadoes. *Science*, **272**, 1774–1777.
- , —, —, M. Randall, and A. Zahrai, 1997: Design and deployment of a portable, pencil-beam pulsed 3-cm Doppler radar. *J. Atmos. Oceanic Technol.*, **14**, 1502–1512.
- , Y. Richardson, C. Alexander, S. Weygandt, and P. F. Zhang, 2007a: Dual-Doppler and single-Doppler analysis of a tornadic storm undergoing mergers and repeated tornadogenesis. *Mon. Wea. Rev.*, **135**, 736–758.
- , —, —, —, and —, 2007b: Dual-Doppler analysis of winds and vorticity budget terms near a tornado. *Mon. Wea. Rev.*, **135**, 2392–2405.
- , P. Robinson, C. Alexander, and Y. Richardson, 2007c: Low-level winds in tornadoes and potential catastrophic tornado impacts in urban areas. *Bull. Amer. Meteor. Soc.*, **88**, 31–46.
- , K. Kosiba, P. Markowski, Y. Richardson, D. Dowell, and P. Robinson, 2010a: Finescale single- and dual-Doppler analysis of tornado intensification, maintenance, and dissipation in the Orleans, Nebraska, supercell. *Mon. Wea. Rev.*, **138**, 4439–4455.
- , L. J. Wicker, Y. P. Richardson, E. N. Rasmussen, P. M. Markowski, D. Dowell, D. W. Burgess, and H. B. Bluestein, 2010b: An overview of the VORTEX2 field campaign. Preprints, *25th Conf. on Severe Local Storms*, Denver, CO, Amer. Meteor. Soc., 5.1. [Available online at https://ams.confex.com/ams/25SLS/techprogram/paper_176068.htm.]
- Zehnder, J. A., J. Hu, and A. Razdan, 2007: A stereo photogrammetric technique applied to orographic convection. *Mon. Wea. Rev.*, **135**, 2265–2277.
- Zrnich, D., and M. Istok, 1980: Wind speeds in two tornadic storms and a tornado, deduced from Doppler spectra. *J. Appl. Meteor.*, **19**, 1405–1415.